Chapter: 6

Electrolytic Capacitorless L_nC_{2n-2} Network-Based Resonant Converter

6.1. Introduction

So far, we have discussed the L_nC_{2n-2} network and its potential for use in the Multi-Output Hybrid Converter (MOHC). One crucial aspect in any power electronic converter is the reliability of its components, and the electrolytic capacitors used in such systems are often the weakest link. Their limited lifespan significantly affects the overall durability of the converter. To address this issue and enhance the reliability and longevity of the L_nC_{2n-2} network, the electrolytic capacitors are replaced with film capacitors. Film capacitors offer greater reliability, higher current density, and a more compact size compared to their electrolytic counterparts, making them a superior choice for this application.

Another important development in DC-DC conversion [122] is the resonant DC-DC converter, which provides an isolation. However, its voltage gain primarily depends on the transformer's turns ratio, limiting its ability to deliver smooth voltage variation. In contrast, integrating the L_nC_{2n-2} network at the input of the resonant converter enables smoother and wider input voltage variation. Furthermore, the voltage gains of the L_nC_{2n-2} network is governed by the duty ratio and can be easily controlled using a single switch, simplifying the control mechanism.

So far, for photovoltaic (PV) applications, considered only the single-peak PV characteristics. However, real-world scenarios often present more complex situations, such as partial shading [123]-[124] of some panels due to obstacles, leading to the formation of multiple peaks in the PV characteristics. Extracting maximum power from these multi-peak characteristics becomes a challenging task. To address this, a Particle Swarm Optimization (PSO)-based algorithm has been applied for global peak tracking. The single-switch control of the L_nC_{2n-2} network further simplifies this task, making the

system highly efficient and easy to manage. This chapter provides a detailed discussion of the implementation and benefits of this approach.

6.2. Expandable Input Impedance Sourced Isolated Resonant Converter

The circuit diagram of the proposed Expandable Input Impedance-Sourced Isolated Resonant Converter (EIISIRC) is presented in Fig. 6.1 This innovative design introduces an electrolytic capacitor-less architecture, making it a highly reliable and long-lasting solution. The converter is seamlessly integrated with solar panels and optimized using a particle swarm optimization (PSO) algorithm to address the challenges of partial shading conditions.

One of the key features of this converter is its expandable impedance-sourced network, which can be scaled up to '*n*' stages. The voltage gain of the system adjusts according to the formula 1/(1 - *nD*), where *D* is the duty ratio and *n* is the number of stages, offering flexible control and adaptability. The EIISIRC also inherits all the well-known benefits of impedance networks, including robust shoot-through protection and strong immunity to electromagnetic interference (EMI).

In addition to these advantages, the converter provides galvanic isolation [125], which is crucial for safe operation and for preventing leakage currents when connected to a grid or inverter system. The inclusion of a resonant tank within the design enhances soft switching capabilities, leading to improved efficiency and reduced switching losses. Furthermore, by utilizing a film capacitor instead of an electrolytic one, the converter achieves greater durability and an extended operational lifespan.

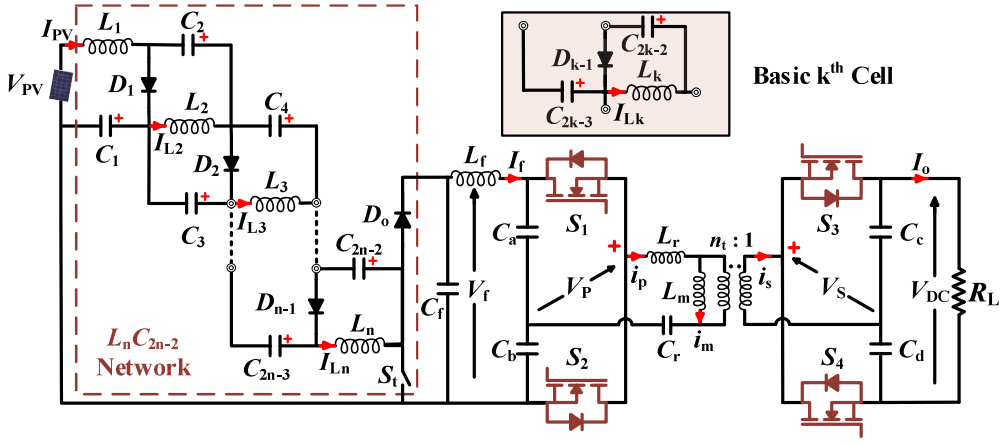

Fig. 6.1 Proposed expandable input impedance sourced isolated resonant converter.

To maximize power extraction from solar panels, especially under complex shading conditions, the EIISIRC employs the PSO algorithm for global maximum power point tracking. This approach effectively overcomes the limitations of traditional methods by accurately identifying the global peak even in the presence of multiple local peaks, ensuring optimal performance and efficiency of the solar power system.

The working principle of the L_nC_{2n-2} network was thoroughly covered in Chapter 2. However, a more in-depth and comprehensive analysis of the proposed expandable impedance network-based isolated resonant converter is provided in the following sections.

6.3. Operation of the Expandable Input Impedance Sourced Isolated Resonant Converter

The operation of the expandable input impedance-sourced isolated resonant converter consists of an expandable impedance network and an isolated resonant converter which is illustrated through three distinct operating intervals I-III. The Waveform of the operation is illustrated in Fig. 6.3, and the operating modes are illustrated in Fig.6.2, and it is explained as follows:

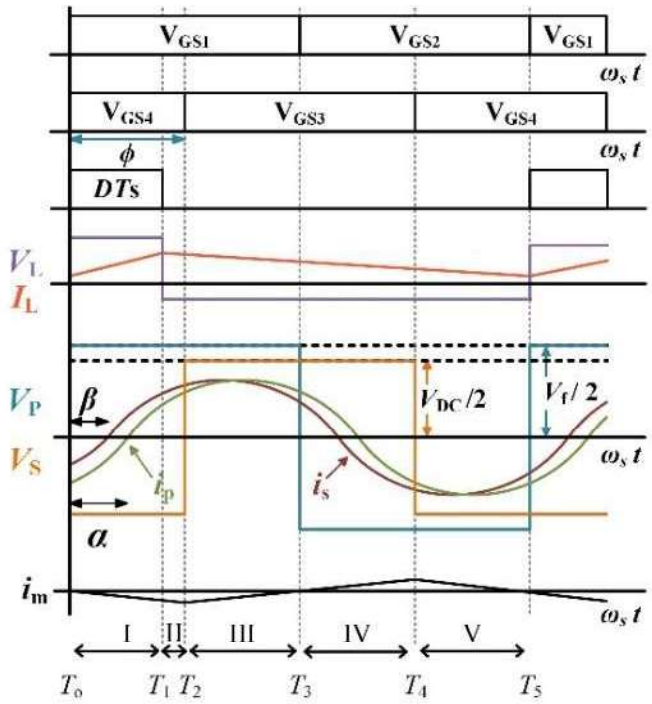

Fig 6.2 Waveforms of the EIISIRC in steady-state condition.

➢ Interval I: ($T_0 - T_1$)

Interval I begins, when switch S_t, receives the gate signal for the duration of the DTs interval, creating a positive voltage across the inductors. As a result, the inductors in the expandable impedance input-sourced (EIIS) network start charging. At the same

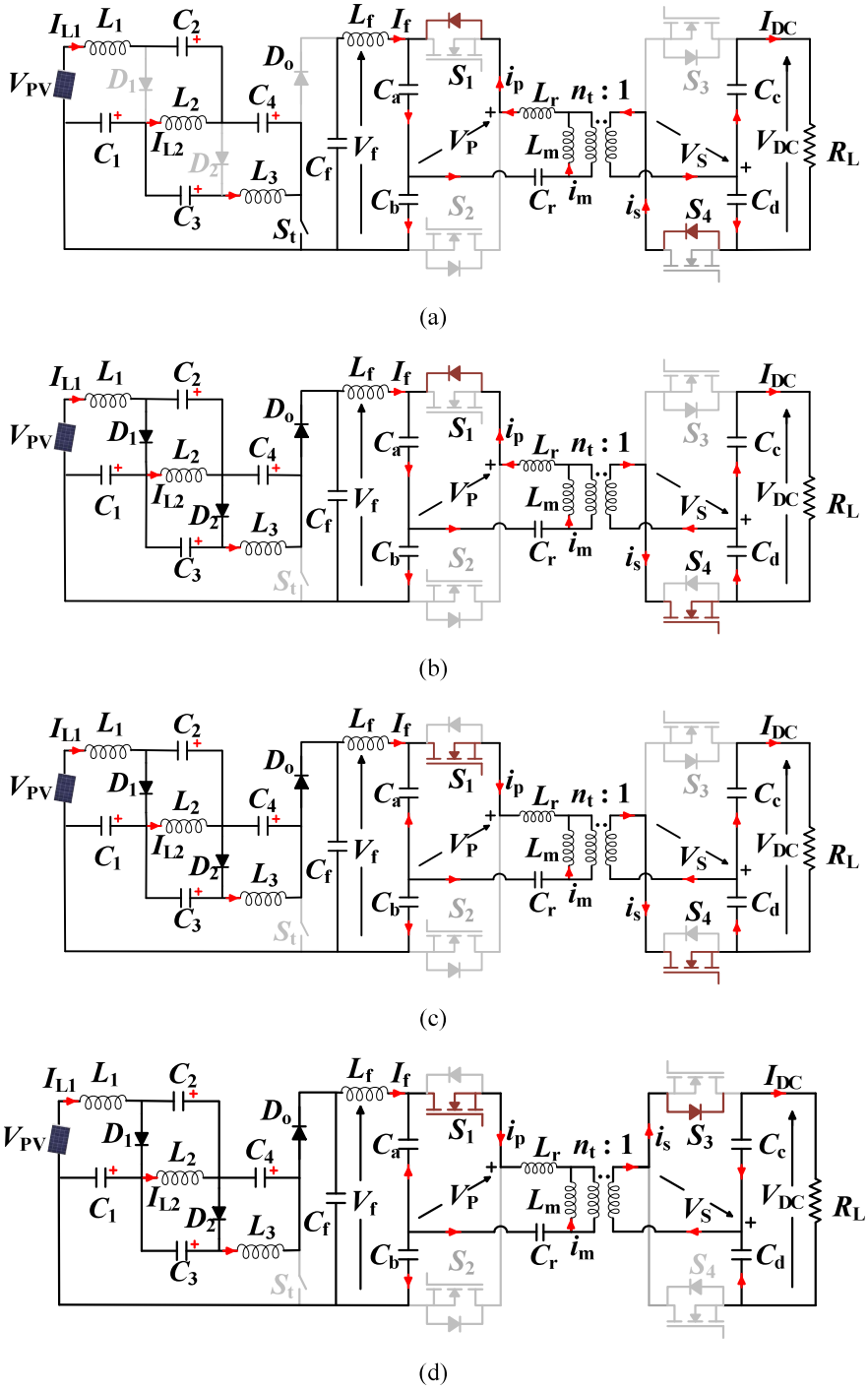

Fig. 6.3. (a)-(d) Equivalent circuit diagram of the proposed EIISIRC in Interval-I to Interval-V.

time, switch S_1 receives its gate signal (V_{GS1}), making the voltage V_P positive. Meanwhile, switch S_4 is already in the on state, which results in a negative voltage V_S.

During this period, the resonant tank begins releasing its stored energy back toward the source, and the body diode of S_1 conducts via the current i_p. Because the voltage $-V_S$ appears across the magnetizing inductance L_m, the current i_m decreases steadily.

On the secondary side of the high-frequency transformer (HFT), the current flows through the dotted terminal of the transformer since i_p is greater than i_m. This current then passes through the body diode of switch S_4, as illustrated in Fig. 6.3(a). As the resonant tank continues releasing energy, the resonant capacitor voltage increases sinusoidally, lagging i_p by 90°.

As i_p decreases and approaches i_m, the secondary-side current rises from zero toward a positive value. This phase reversal happens at $\omega_{st} = \beta$ when switch S_4 conducts, as shown in Fig. 6.3(b). Once the system reaches $\omega_{st} = \alpha$, the resonant tank starts storing energy again, and i_p begins increasing from zero in the positive direction.

When i_p reverses direction, switch S_1 starts conducting, as depicted in Fig. 6.3(c). Since the body diodes of the active switches (S_1 and S_4) conduct before the switches themselves turn on, both switches operate with zero-voltage switching (ZVS), ensuring efficient and low-loss operation.

➢ Interval II: ($T_1 - T_2$)

Interval II starts when switch S_t stops receiving gate signals, which causes the inductors in the expandable impedance input-sourced (EIIS) network to begin discharging during the remaining part of the switching cycle. During this phase, the stored energy in the inductors is released, driving the circuit's operation.

Apart from this change, the rest of the converter's behaviour remains similar to what was observed in Interval I, continuing the energy transfer and maintaining the same switching dynamics and resonant behaviour.

➢ Interval III: ($T_2 - T_3$)

Interval III begins when the gate signal V_{GS4} is removed from switch S_4 and V_{GS3} is applied to switch S_3, causing the bridge voltage V_S to become positive. Given the

direction of the secondary current is, the body diode of S_3 starts conducting, as illustrated in Fig. 6.3(d).

Since the switching operation is symmetrical in the second half of the cycle, the behavior in the following intervals (IV and V) mirrors the processes described in the earlier intervals. This symmetry simplifies the analysis, as the same principles apply to the remaining half of the switching period.

6.4. Design of the Expandable Input Impedance Sourced Isolated Resonant Converter

To ease the design calculation, the base parameters selected for the proposed converter are as follows:

$$V_B = V_f, Z_B = \sqrt{\frac{L_r}{C_r}} \text{ and } \omega_B = \omega_r \tag{6.1}$$

Here, V_B, Z_B, and ω_B denote the base voltage, base impedance, and base angular frequency in rad/sec. Using the above-mentioned base parameters, the resonant tank components can be normalized in per-unit values as follows:

$$X_{Lr,pu} = F, X_{Cr,pu} = 1/F, \text{ and } X_{Lm,pu} = F/K \tag{6.2}$$

For a given switching frequency (ω_s) and resonant frequency (ω_r), the normalized switching frequency (ξ) can be given as:

$$\xi = \frac{\omega_s}{\omega_r} \tag{6.3}$$

The design of a 500 W prototype with an input voltage of 60 V, delivering an output voltage of 120 V, considering a DC link voltage of 120 V with a ±2.5% ripple factor. The proposed converter is designed to efficiently harness solar power within an input voltage range of 50 V to 70 V. Based on these specifications, the key parameters of the proposed topology can be determined as follows:

6.4.1. Normalized Switching Frequency (ξ)

Selecting an appropriate normalized switching frequency plays a crucial role in enabling the converter to operate with soft-switching, which helps reduce switching losses and improves overall efficiency. In addition, minimizing conduction losses requires careful optimization of the resonant currents, which depend on the parameter ξ.

For this design, considering both the need for soft-switching and minimizing losses under fixed-frequency operation, the value of ξ is set to 1.2. This choice ensures optimal performance by balancing efficient energy transfer and reduced power dissipation.

6.4.2. Gain (λ), turns ratio (n_t), and Inductance Ratio (K)

Based on the modelling discussed earlier, it can be concluded that for the converter to achieve zero-voltage switching (ZVS), the voltage gain λ must be less than or equal to 1. Therefore, the maximum value of λ should be unity.

To achieve a higher DC link voltage when needed, the transformer turns ratio n_t can be adjusted accordingly. Given the known constraints on the converter's voltage gain, the turns ratio can be expressed as shown in equation (6.1).

$$n_t = \frac{\lambda_{max} V_f}{V_{DC}} \tag{6.4}$$

Similarly, using (6.1), the minimum converter gain (for V_{DC} = 120 V - 2.5 %) and corresponding inductance ratio can be calculated using (6.2) from the no-load condition as K = 0.1678.

$$\lambda > \frac{cos\,\phi}{X} \tag{6.5}$$

6.4.3. Quality Factor

The quality factor plays a key role in deciding the size of the resonating components and the current through them. For a resonant converter, the size of the reactive component is proportional to the quality factor. So, a small value of a quality factor is expected. In Fig. 6.4(a), the converter gain vs. phase-shift angle curve is shown. It can be seen from the curve that for a low value of the quality factor, the converter gain increases rapidly, which is undesirable. To operate the converter with ZVS, the primary current angle (alpha) vs phase shift angle curve is drawn and shown in Fig. 6.4(b). It can be observed from Fig. 6.4(b) that when the quality factor is less than 2, the zero-voltage switching will be lost. As the quality factor can't be a large value and for less than 2, zero voltage switching operation is lost, so an optimum value of 2 is selected for the operation of the proposed converter.

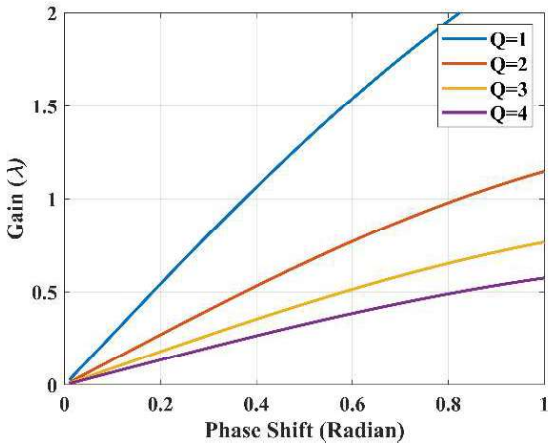

(a)

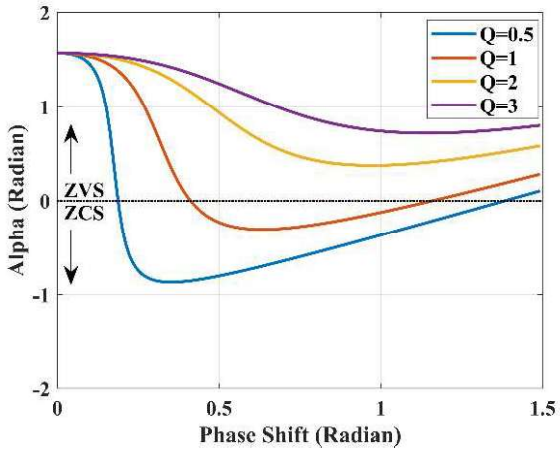

(b)

Fig. 6.4. Variation of (a) Converter gain (λ) and (b) Angle alpha presenting ZVS range with phase shift angle (Radian) for different values of the quality factor.

6.4.4. Resonant Components

Now, as the critical parameters are decided, the tank parameters can be determined as follows:

$$L_r = \frac{\xi Z_B}{2\pi f_s},\ L_m = \frac{L_r}{K} \text{ and } C_r = \frac{\xi}{2\pi f_s Z_B} \tag{6.6}$$

6.4.5. Design of the EIIS Network Inductors

For $n = 3$ stages, since the current through each inductor remains constant, the inductors are designed by considering the ripple factor (%RF). The specific design for this case is as follows:

$$L_r = \frac{\xi Z_B}{2\pi f_s},\ L_m = \frac{L_r}{K} \text{ and } C_r = \frac{\xi}{2\pi f_s Z_B} \tag{6.7}$$

Similarly, the inductor for n stage EIIS can be calculated by:

$$L_1 = L_2 \ldots\ldots\ldots = L_n = \frac{D(1-D)V_{PV}}{f_s(1-3D)(\%RF)I_{L1}} \tag{6.8}$$

6.4.6. Design of Film Capacitors of the EIIS Network

To replace the electrolytic capacitor with the film capacitor, the current carrying capacity per unit capacitance property for the required voltage rating is considered [120]. The film capacitor has an RMS current rating of 1 A/μF. The film capacitors must carefully determine the minimum capacitance required for the given system. The minimum capacitance (C_k) value needed to handle the rms value of capacitor current (I_{cap}) at a switching frequency (f_s), while maintaining a required voltage ripple factor (%RF) for capacitor voltage C_k and can be expressed as:

$$(C_k)_{min} = \frac{I_{cap}}{2\pi f_s(\%RF)V_{ck}} \tag{6.9}$$

Where, k = 0, 1, 2……(2n-2).

6.4.7. Design of Film Capacitors (FCs) of IRC

The FCs (C_a and C_b) take part in the resonance operation and are responsible for generating square signals across the bridge voltages. To eliminate the noise on the input side, the input FCs are calculated for a 2% ripple in V_{PV} as follows:

$$C_a = C_b = \frac{[I_{PV}(\pi-\phi)-i_{pm}(\cos\alpha+\cos(\phi-\alpha))]}{\omega_s \Delta V_{C_1}} \tag{6.10}$$

Further, it is also desirable that C_a and C_b be equal and too large than the resonance capacitance C_r to avoid resonating interference. So,

$$C_a = C_b >> 100C_s \tag{6.11}$$

Based on the above constraints in (6.10)-(6.11), C_a and C_b of equal value 20 μF are selected.

Similarly, assuming the output current is ripple-free, the current via C_c and C_d when the switch S_3 is turned off will be equal to the output current for a duration of half the switching cycle. The ripple voltage of the C_c and C_d can be calculated as:

$$\Delta V_{C_c} = \Delta V_{C_d} \approx \frac{1}{C_3}\int_0^{T_s/2} I_{DC}\, dt \tag{6.12}$$

Algorithm 6.1 PSO-based Maximum Power Point Tracking

Input: Input Voltage and input current.

Initialization: Swarm size (n), position vectors (x_i), velocity vectors (v_i), inertia constant (ω), weighting factors (c_1 and c_2), and random numbers (r_1, and $r_2 \in (0,1)$).

Global Optimization

1: For the given sampling time and each particle, input voltage and input current are sensed, and power is calculated.
2: The power value (Personal best P_b) is updated for each swarm only if the current value of power is greater than the previous value; otherwise, it remains the same.
3: At the end of each iteration, the personal best of each particle is compared with the previous global best (G_b), and G_b is updated only if it is lesser than the current personal best value of any swarm.
4: Based on steps 2 and 3, update each particle's position and velocity vectors using (21) and (22).
5: Repeat steps 1 to 4 until the algorithm is converged and global peak power is achieved.

Output: Based on the value of the G_b, Generate the duty cycle "D".

$$C_c = C_d = \frac{I_{DC}}{2\omega_s \Delta V_{C_3}} \tag{6.13}$$

From (6.13), the C_c and C_d are chosen to be approximately 20 μF.

Based on the given design calculation, the film capacitors are chosen from the MKP1848H series [126] and compared with the electrolytic capacitor series [127]. It is evident that the film capacitors are 10 times more compact than the electrolytic capacitor for the same voltage and current per unit capacitance rating.

6.5. PSO Algorithm for the Partial Shading Conditions

Particle swarm optimization is a swarm foraging-inspired computational technique discovered by Russell Eberhart and James Kennedy in 1995 [128]-[130]. The development of the PSO involves basic vector operation leading to a fast-converging algorithm. In PSO, the particles are denoted as a candidate solution and represented as a position (x_i) and velocity vector (v_i). These particles learn and update using their experience and experience of the swarm. Every candidate has a best position (P_{bi}) based on their experience. Similarly, there is a global best of the whole swarm (G_b). The position and velocity updates as per the mathematical equation given as:

$$v_i^{k+1} = wv_i^k + c_1r_1(P_{bi}^k - x_i^k) + c_2r_2(G_b^k - x_i^k) \quad (6.14)$$

$$x_i^{k+1} = x_i^k + v_i^{k+1} \quad (6.15)$$

For i = 1, 2, 3…. n (No. of particles).

Where k denotes the iterations and v_i^{k+1} and v_i^k is the velocity of particle i at iteration k+1 and k, x_i^{k+1} and x_i^k is the position of particle i at iteration k+1 and k, w is the inertia coefficient of particle, c_1 and c_2 are constant weighting factor, r_1 and r_2 are the random numbers (chosen between 0 and 1). c_1 and c_2 are cognitive and social learning coefficient that tries to move the particle towards personal and global best, respectively. The step-by-step operation for the PSO-based MPPT algorithm used for the proposed converter is shown in Algorithm 6.1.

6.6. Comparative analysis

The field of isolated DC-DC converters has seen significant advancements, with various topologies proposed to address voltage gain, reliability, and integration with solar photovoltaic (PV) systems. This comparative analysis illustrated in Table 6.1 evaluates the proposed topology against existing designs, highlighting their strengths, limitations, and suitability for solar PV applications.

Existing topologies, such as those presented in [109]-[118], often rely on electrolytic capacitors, which are known for their vulnerability and limited lifespan. This directly impacts the overall reliability and longevity of the converters. Among these, [109]-[116] introduce impedance-based isolated DC-DC converters; however, they have not been validated for solar PV integration. This lack of verification raises concerns about their compatibility with renewable energy sources, particularly in scenarios requiring maximum power point tracking (MPPT).

The topology proposed in [113] achieves the highest efficiency among the referenced designs, yet it lacks soft-switching capabilities. This absence of soft switching increases component stress, leading to higher power losses and reduced system durability. Additionally, [113] continues to employ electrolytic capacitors and does not demonstrate compatibility with solar PV systems, as it fails to implement any MPPT algorithm for single- or multi-peak PV characteristics.

Although [114] offers higher voltage gain characteristics, its design lacks expandability and does not support soft switching. This results in increased stress on active

TABLE 6.1

COMPARATIVE ANALYSIS OF ISOLATED RESONANT CONVERTER

Parameters	[109]	[110]	[111]	[112]	[113]	[114]	[115]	[116]	[117]	[118]	Proposed
Switches	4	2	4	4	4	4	5	8	5	4	5
Diodes	4	3	3	3	4	7	6	0	2	4	3
Inductors	1	2	2	2	1	3	2	2	0	1	5
Capacitors	3(EC)	7 (EC)	4(EC)	4(EC)	3(EC)	3(EC)	3(EC)	3(EC)	4(EC)	4(EC)	10(FC)
Transformers	1	1	1	1	1	1	1	1	2	1	1
Voltage Gain	$\frac{2n_t}{(1-2D)}$	$\frac{n_t}{(1-2D)}$	$\frac{2}{n(1-2D)}$	$\frac{n_t}{(1-2D)}$	$\frac{2n_t}{(1-2D)}$	$\frac{n_t}{4(1-D)^2}$	$\frac{n_t}{2(1-D)}$	$\frac{n_t}{(1-2D)}$	$\frac{2n_t}{(1-2D)}$	n_t	$\frac{M}{(1-nD)}$
Soft Switching	Yes	yes	No	yes	No	No	No	No	Yes	Yes	Yes
Peak Efficiency	95.5%	NA	95%	89.06%	98.7%	95.9%	94.6%	NA	95%	95.8%	96.05%
Solar PV Integration	No	No	No	No	No	No	No	No	Yes	Yes	Yes
Algorithm	×	×	×	×	×	×	×	×	ST-MPPT	P&O	PSO
Time to reach GMPP	×	×	×	×	×	×	×	×	3s	×	0.72s

components and higher switching losses. Moreover, [114] has not been tested for solar PV integration, further limiting its practical application in renewable energy systems.

Only [117] and [118] incorporate solar PV integration, yet both have significant limitations. The topology in [117] uses a grid-tied inverter and a quasi-Z-source (qZS) series resonant DC-DC converter equipped with Shade Tolerant MPPT (ST-MPPT) to track global maxima under partial shading conditions. While effective, this approach requires two transformers, adding complexity and cost to the system design. On the other hand, [118] integrates solar PV but depends solely on the transformer turn ratio to achieve voltage gain. This reliance limits its adaptability to wide input voltage variations. Furthermore, [118] employs the perturb and observe (P&O) algorithm, which is only effective for systems with single-peak PV characteristics and struggles with dynamic environmental changes.

The proposed topology overcomes these limitations by combining the benefits of isolated and non-isolated converters. It uses a single transformer and eliminates the need for electrolytic capacitors, enhancing reliability and lifespan through the use of robust film capacitors. Additionally, the converter achieves a peak experimental efficiency of 96.05%, comparable to the highest-performing designs while maintaining reduced component stress and improved soft-switching capabilities.

A key innovation in the proposed topology is the implementation of Particle Swarm Optimization (PSO) for MPPT. PSO, inspired by swarm foraging behaviour and developed by Russell Eberhart and James Kennedy in 1995, is a fast-converging

TABLE 6.2

DESIGN PARAMETERS OF EIISIRC AND PSO

Parameters	Value	Parameters	Value
Input PV Voltage (V_{PV})	60 V	Particles	3
Output Voltage (V_{DC})	120 V	w	0.4
Output Power (P_{DC})	500 W	c_1	1.45
Switching Frequency (f_s)	50 kHz	c_2	1.63
Resonant inductor (L_r)	60.68 µH	r_1 and r_2	(0,1)
Parallel inductor (L_m)	292 µH	n_t	28:25
Resonant capacitor (C_r)	240.43 nF	C_a-C_d	20 µF
Inductors (L_1, L_2, and L_3)	560 µH	C_2-C_4	15 µF
C_1	20 µF	C_f	25 µF

optimization technique based on simple vector operations. In this approach, each particle represents a candidate solution defined by its position and velocity. Particles update their positions based on their own best experiences and the global best position of the swarm, leading to efficient exploration and exploitation of the solution space. This allows PSO to track the maximum power point quickly and accurately, outperforming traditional methods like ST-MPPT and P&O, particularly in systems with multi-peak PV characteristics and partial shading conditions.

In conclusion, the proposed topology offers a more efficient, reliable, and adaptable solution for solar PV applications. By eliminating electrolytic capacitors, supporting soft switching, and employing the faster and more robust PSO algorithm, it addresses the limitations of existing designs while achieving high efficiency and longevity. These advancements make it well-suited for renewable energy systems operating across a wide input voltage range.

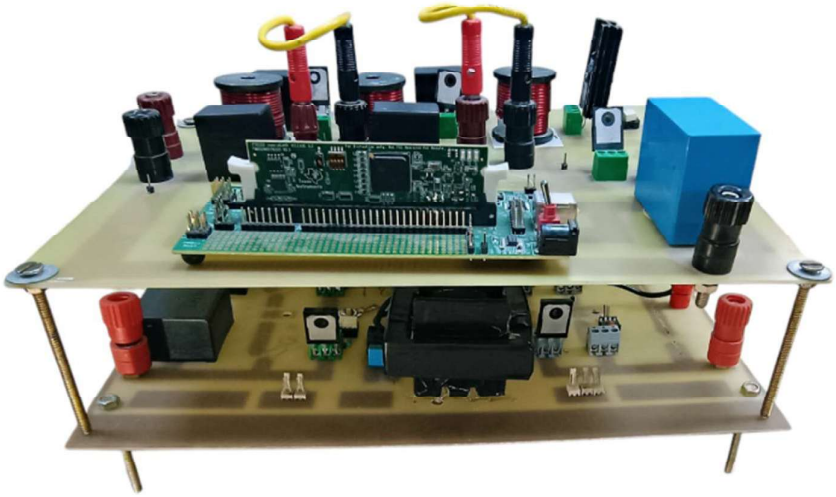

Fig. 6.5. Photograph of experimental Setup.

6.7. Experimental Validation

For the experimental validation of the proposed EIISIRC, a 500 W laboratory prototype was built and thoroughly tested. The testing process covered various operating conditions, including steady-state performance, soft-switching capability, uniform irradiance conditions (UIC), and partial shading conditions (PSCs). A photograph of the developed experimental prototype is presented in Fig. 6.5, providing a clear view of the setup. The key design parameters used in the experimental configuration, along with those applied in the PSO algorithm, are detailed in Table 6.2. To emulate the PV characteristics, we used Chroma's 62100H-600S solar PV emulator, ensuring accurate replication of real-world solar conditions. The control algorithm was implemented on Texas Instruments' TMS320F28335 microcontroller, a widely used experimental kit known for its efficiency and reliability in power electronics applications.

6.7.1. Steady State Results for Proposed Expandable Input Impedance Sourced Isolated Resonant Converter

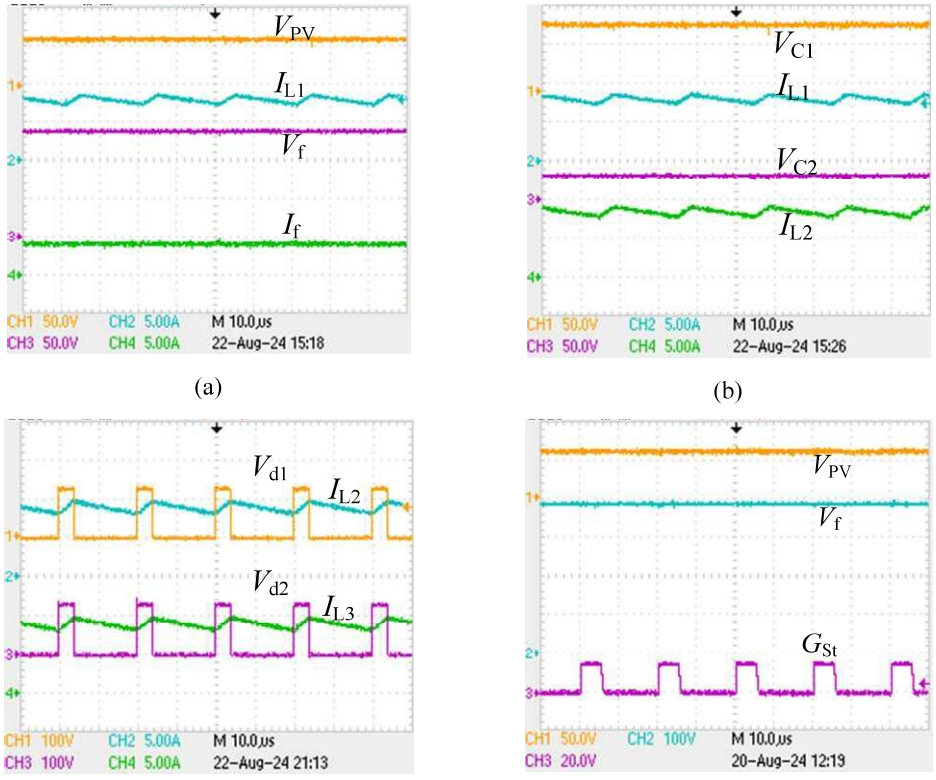

Fig. 6.6. Steady-state results of EIISIRC (a) Input and output characteristics. (b) Charging and discharging of capacitor voltage and inductor current of EIIS network (c) Voltage stress across diodes and inductor current of EIIS network. (d) The high gain capability of the EIIS network.

Fig. 6.6 provides a comprehensive overview of the EIISIRC system's performance under various operating conditions. In Fig. 6.6(a), the system operates with an input PV voltage of 60 V and an inductor current (I_{L1}) of 8.33 A, successfully delivering an output voltage of 140 V and an output current of 3.4 A. This demonstrates the system's effective power conversion capability.

Fig. 6.6(b) captures the voltage and current stresses across the impedance network components, where the capacitor voltages are measured as V_{C1} = 86 V and V_{C2} = 26 V, highlighting the balanced voltage distribution within the network.

In Fig. 6.6(c), the voltage stress across the diodes is illustrated, showing V_{d1} and V_{d2} both at 120 V, accompanied by the inductor current waveform. This observation confirms the system's ability to manage voltage stress efficiently while maintaining stable current flow.

Finally, Fig. 6.6(d) showcases the remarkable high-voltage gain capability of the EIIS network. With an input voltage of 60 V and a duty cycle of D = 0.28, the network

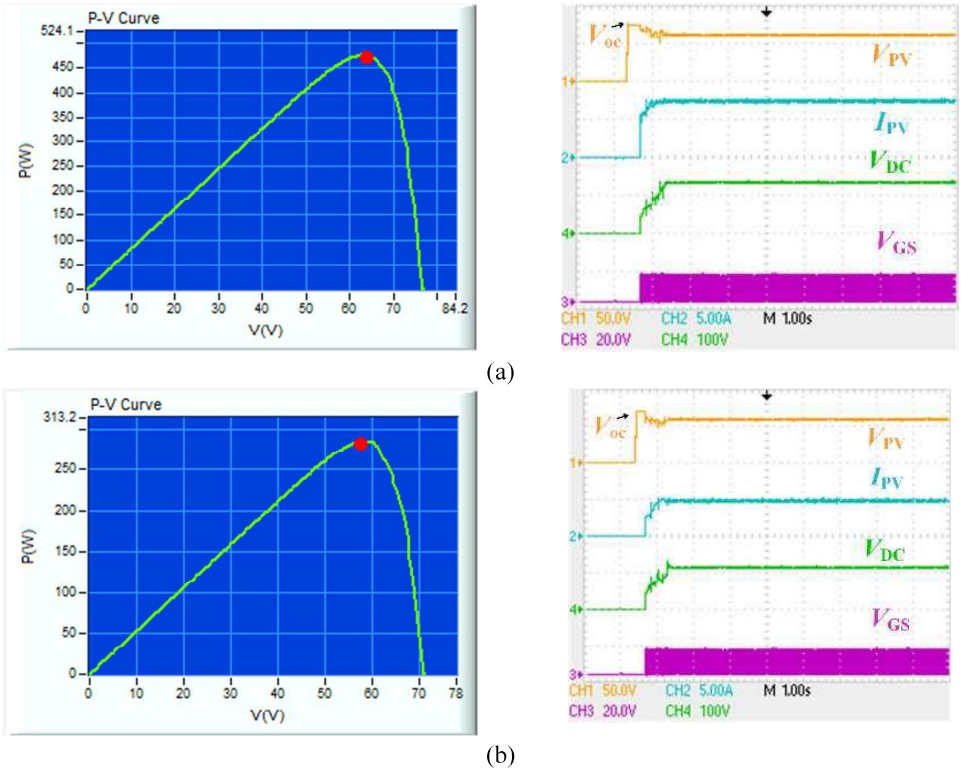

Fig. 6.7. The generated PV curves by the solar PV emulator, along with the corresponding experimental results, illustrate the input voltage, input current, and output voltage with the gate signal V_{GS1} for (a) PVC-1 and (b) PVC-2.

successfully boosts the voltage up to 390 V. This impressive voltage gain underlines the system's potential for high-efficiency power conversion in PV applications.

6.7.2. Results Under Uniform Irradiance Conditions

To demonstrate the effectiveness of the PSO algorithm, two distinct PV curves, PVC1 and PVC2, were emulated using a PV emulator under uniform irradiance conditions. PVC1 achieves a peak power of 476.4 W at an operating voltage of 62.7 V, with an open circuit voltage (V_{oc}) of 76.5 V, as illustrated in Fig. 6.7(a). The PSO algorithm successfully tracks the maximum power point in approximately 0.72 seconds, as depicted in the same figure.

Similarly, PVC2 reaches a peak power of 284.8 W at 58 V, with a V_{oc} of 70.9 V, as shown in Fig. 6.7(b). In this case, the algorithm takes around 0.64 seconds to identify the peak power point, clearly demonstrating its rapid and efficient performance.

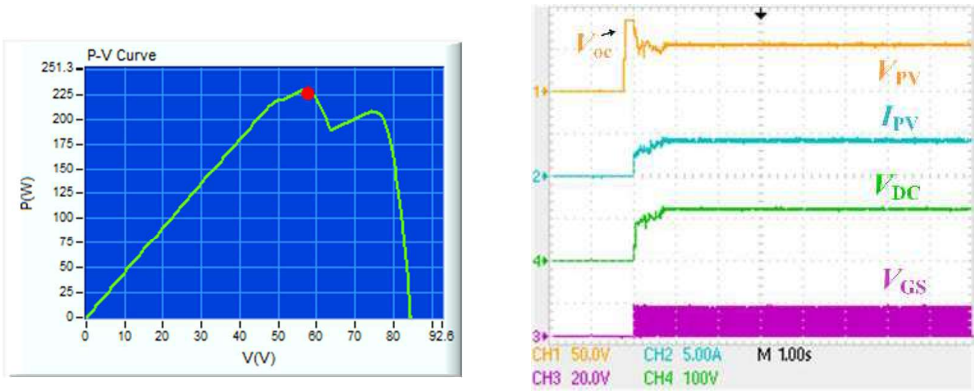

(a)

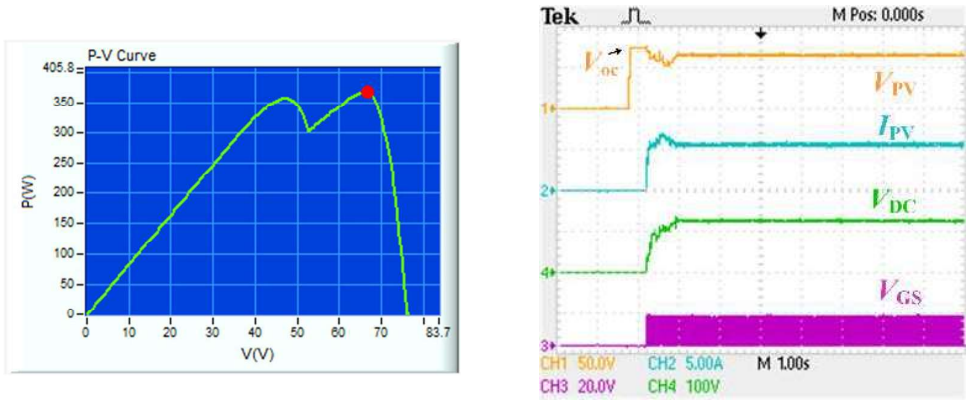

(b)

Fig. 6.8. The generated PV curves by the solar PV emulator, along with the corresponding experimental results, illustrate the input voltage, input current, and output voltage with the gate signal V_{GS1} for (a) PSC-1 and (b) PSC-2.

These results highlight the algorithm's ability to quickly and accurately detect the optimal power points across different PV characteristics, making it well-suited for real-time solar energy applications.

6.7.3. Results Under Partial Shading Conditions and Dynamic Irradiance Conditions

To evaluate the performance of the proposed system under partial shading conditions (PSCs), three distinct PV characteristics (PSC-1 to PSC-3) are emulated using a solar PV emulator. Let's take a closer look at the behaviour of each curve.

For PSC-1, the PV curve features a global maximum power (GMP) of 228.5 W, achieved at a voltage of 55.7 V, with an open-circuit voltage (V_{oc}) of 84.2 V, as illustrated in Fig. 6.8(a). Additionally, a local maximum power (LMP) of 207.6 W is observed at 74.32 V. The algorithm demonstrates its efficiency by detecting the GMP point in approximately 0.76 seconds, as depicted in Fig. 6.8(a).

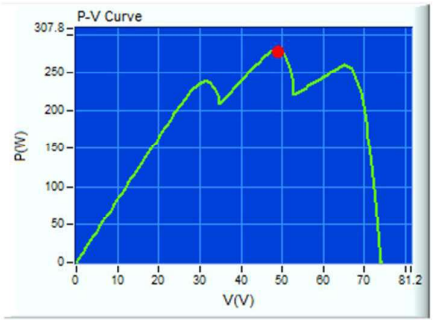

(a)

(b)

(c)

Fig. 6.9. Experimental results showing dynamic irradiance (a) PSC-3. (b) Change in shading patterns from PSC-2 to PSC-3 (c) Change in shading patterns from PSC-3 to PSC-1 showing input voltage, input current, and output voltage with gate signals V_{GS1}.

Moving on to PSC-2, the curve exhibits a higher GMP of 368.9 W at 66.5 V, with an open-circuit voltage of 76 V, shown in Fig. 6.8(b). In this case, the LMP is slightly lower, measuring 356.1 W at 47.51 V. The algorithm identifies the GMP point even faster in this scenario, taking just 0.72 seconds, as shown in Fig. 6.8(b).

These results highlight the algorithm's effectiveness in quickly and accurately locating the global maximum power point under different shading conditions, ensuring optimal performance of the PV system.

Moreover, For dynamic irradiance behavior, the shading pattern is changed from PSC-2 to PSC-3 and PSC-3 to PSC-1. PSC-3 has a GMP of 279.8 W at 48.9 V with a V_{oc} of 73.9 V, as shown in Fig. 6.9(a). The experimental results corresponding to the dynamic change in irradiance are shown in Fig. 6.9 (b)-(c). When PSC-2 is applied, the duty varies to detect the GMP, and it takes approximately 6-8 iterations to reach GMP. When a change in irradiance is sensed due to a change in shading pattern, the duty cycle varies to search for the new global peak power again. The algorithm repeats the process till the convergence is achieved. A similar process can be observed when the shading pattern is changed from PSC-3 to PSC-1. It can be concluded from the experimental results of the UIC and PSC tests that the algorithm tracks the peak power with no oscillation in steady-state waveforms.

6.7.4. Verification of Film Capacitor Usage

Fig. 6.10 provides a comprehensive evaluation of the performance of film capacitors (FCs) in the proposed EIISIRC configuration, offering a clear comparison with conventional electrolytic capacitors. The results highlight the distinct advantages of film capacitors, particularly in terms of reliability, longevity, compactness, and power density — all critical factors in power electronics applications.

To validate the practical suitability of film capacitors, voltage measurements were conducted across the capacitors under various operational scenarios, including startup transients, dynamic load changes, and steady-state conditions. These performance results are illustrated in Fig. 6.10(a)-(d).

In Fig. 6.10(a), the behaviour of the film capacitors is observed during a sudden 50% increase in load. This figure specifically captures the voltage response of the DC-link capacitors (C_c and C_d) along with the capacitors in the EIIS network (C_1 and C_2),

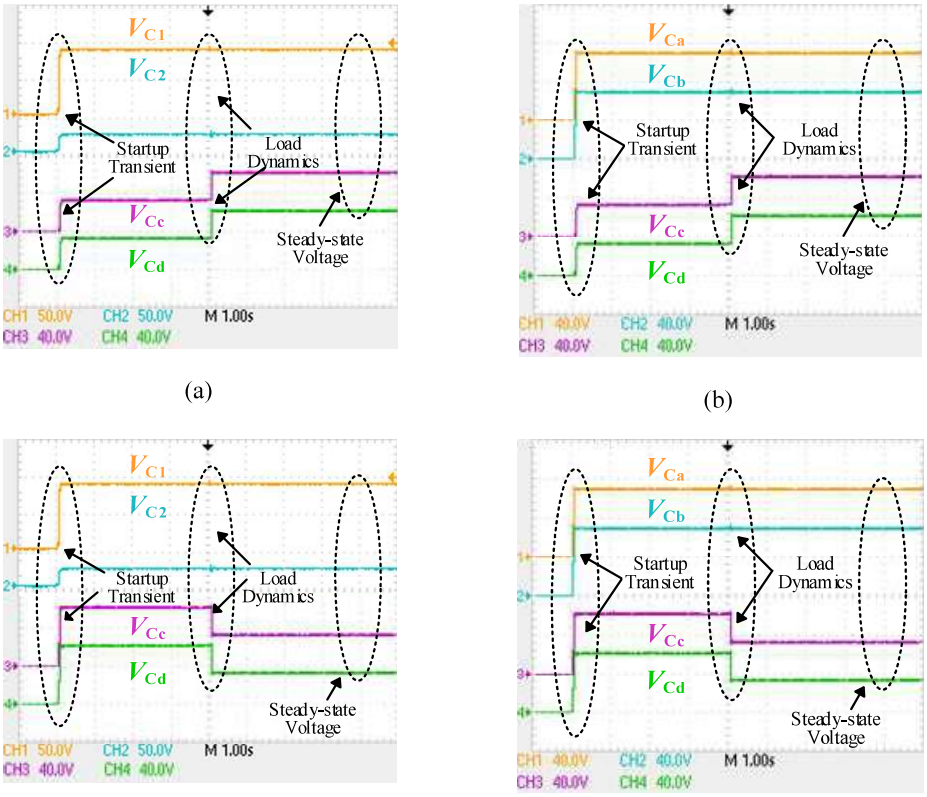

Fig. 6.10. Film capacitor voltages during startup transients, load dynamics, and steady-state conditions (a) V_{C1}-V_{C2} and V_{Cc}-V_{Cd} voltage for 50% step load increase (b) V_{Ca}-V_{Cd} voltage for 50% step load increase (c) V_{C1}-V_{C2} and V_{Cc}-V_{Cd} voltage for 50% Step Load Increase and (d) V_{Ca}-V_{Cd} voltage for 50% step load Decrease

showing how they handle abrupt load variations. Similarly, Fig. 6.10(b) presents the voltage dynamics of the DC-link capacitors (C_a and C_b) in conjunction with the capacitors of the IRC (C_c and C_d) under the same load change conditions. Fig. 6.10(c) and 6.10(d) further demonstrate the consistent performance of the film capacitors when subjected to a 50% load step increase.

A key takeaway from these experimental results is the remarkable voltage stability of film capacitors. Despite sudden and significant load variations, the FC voltages remain steady and exhibit minimal oscillations. This stability underscores the robustness of film capacitors and confirms their practicality for deployment in the EIISIRC system. The combination of superior electrical characteristics and resilience to dynamic operating conditions makes FCs an ideal choice for enhancing system performance and reliability.

6.8. Loss and Efficiency Analysis

The loss distribution curve and the efficiency curve of the proposed converter are depicted in Fig. 6.11(a) and Fig. 6.11(b), respectively. The primary sources of power losses in the system arise from the active switching devices, passive components used for resonance and filtering, diodes, and the high-frequency transformer. Based on theoretical analysis, the converter is expected to achieve a peak efficiency of 97.2%. However, experimental validation reveals a slightly lower peak efficiency of 96.05%, recorded at an output power of 300 W. This small deviation is primarily due to non-idealities and inaccuracies in the circuit parameters of the experimental prototype, which are difficult to eliminate completely in practical implementations. Additionally, the loss distribution curve, shown in Fig. 6.11(b), provides a detailed breakdown of power losses at an output power of 500 W, offering further insights into the contribution of each component to the overall efficiency of the system.

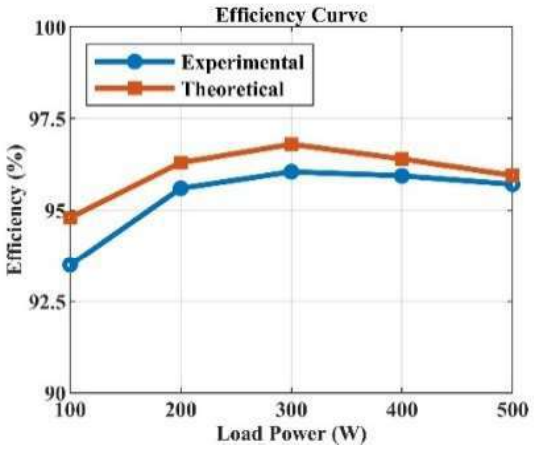

(a)

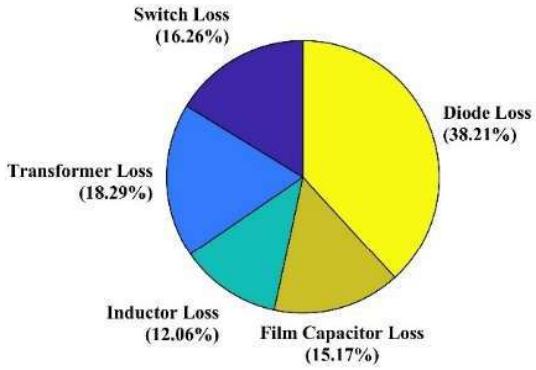

(b)

Fig. 6.11. (a) Efficiency Curve (b) Loss distribution curve at 500 W for the proposed converter.

6.9. Summary

In this chapter, an innovative electrolytic capacitorless isolated resonant converter, based on the L_nC_{2n-2} network, has been proposed. The chapter provides a comprehensive discussion of the working principles of the converter and its detailed design methodology and found that the L_nC_{2n-2} network based expandable impedance network is suitable for the resonant converter.

One of the key challenges addressed in this work is the efficient tracking of the global maximum power point (GMPP) under multi-peak power-voltage characteristics, which is often encountered in photovoltaic systems. To overcome this, a Particle Swarm Optimization (PSO)-based algorithm has been implemented, ensuring accurate and fast GMPP tracking.

The performance of the proposed converter has been thoroughly compared with various existing topologies, and the results demonstrate its superior efficiency and faster tracking capabilities. To further validate the effectiveness of this approach, a 500 W experimental prototype was developed and tested. Finally, the chapter presents an analysis of the converter's overall efficiency and loss distribution, highlighting its practical feasibility and performance benefits.